Thin Solid Films 517 (2009) 1922–1927

Contents lists available at ScienceDirect

Thin Solid Films

journal homepage: www.elsevier.com/locate/tsf

Investigation of microstructure and mechanical properties of multi-layer Cr/Cr_2O_3 coatings

Xiaolu Pang [a], Kewei Gao [a,*], Fei Luo [a], Yusuf Emirov [b], Alexandr A. Levin [c], Alex A. Volinsky [d]

[a] Department of Materials Physics and Chemistry, University of Science and Technology Beijing, Beijing 100083, China
[b] Nanotechnology and Nanomanufacturing Research Center, University of South Florida, Tampa FL 33620, USA
[c] Institut für Strukturphysik, Technische Universität Dresden, 01062 Dresden, Germany
[d] Department of Mechanical Engineering, University of South Florida, Tampa FL 33620, USA

ARTICLE INFO

Article history:
Received 24 January 2008
Received in revised form 6 September 2008
Accepted 3 October 2008
Available online 18 October 2008

Keywords:
Chromium oxide
Multi-layer
Microstructure
Fracture toughness
Adhesion

ABSTRACT

Single and multi-layer Cr/Cr_2O_3 coatings were deposited by reactive magnetron sputtering with the total thickness of 7 μm on steel substrates. X-ray diffraction analysis showed that single and multi-layer Cr/Cr_2O_3 coatings have different preferred crystal orientations. Columnar microstructure was detected by transmission electron microscopy both in metal chromium and ceramic chromium oxide layers. Grain size increased with the coating thickness. The value of single and multi-layer coating's fracture toughness is between 4 and 6 $MPa{\cdot}m^{1/2}$ measured with the Berkovich tip indentation, and it is between 2.8 and 3.9 $MPa{\cdot}m^{1/2}$ when measured with the Vickers indenter. The adhesion is about 192.1 and 246.7 J/m^2 for single and multi-layer coatings, respectively.

1. Introduction

Chromium oxide exhibits good optical, magnetic and mechanical properties, so it can be used as a selective solar ray collector and for other applications as a protective coating against wear, corrosion, and oxidation [1–6]. Among various chromium oxides, Cr_2O_3 is most chemically stable under ambient conditions [7]. The performance and reliability of chromium oxide coatings is often limited by their mechanical properties. Nanoindentation methods are routinely used for elastic modulus and hardness coatings characterization, although the main chromium oxide coatings failure model is fracture and delamination, thus it is important to investigate the coating fracture toughness and adhesion properties. Up to now, there has been no discussion of chromium oxide coatings fracture toughness in the literature.

Various techniques have been used to deposit Cr_2O_3 coatings, including sputtering [1,2,4,8–10] electron-beam evaporation [11,12], chemical vapor deposition [6,7], electrochemical deposition [13], and chemical spray pyrolysis [14], based on different applications. Various deposition methods result in different chromium oxide coatings microstructure, which controls their properties, so it is important to know the microstructure of specimens prepared by different deposition methods. Magnetron sputtering has become the process of choice for the deposition of a wide range of industrially important coatings. Examples include hard, wear-resistant, low friction, corrosion resistant, decorative coatings and coatings with special optical or electrical properties. Quality films and coatings can be deposited by magnetron sputtering, but unfortunately they are typically highly stressed. With the increase of coating thickness, the residual stress typically increases. Several studies showed that coating thickness plays an important role in enhancing both physical vapor deposition (PVD) coated tool cutting performance and resistance to abrasive and erosive wear [15]. Graded systems have been employed to obtain thicker coatings without losing performance in terms of coating adhesion and fracture toughness [16]. It is also likely that thicker coatings will improve corrosion resistance in aqueous environments by eliminating through-thickness pin-hole defects.

In this paper X-ray diffraction (XRD) and transmission electron microscopy (TEM) techniques were used to characterize the microstructure of multi-layer chromium oxide coatings prepared by reactive radio frequency magnetron sputtering technique. Fracture toughness and adhesion were also investigated.

2. Experimental details

Chromium oxide coatings were deposited on $W_{18}Cr_4V$ high speed steel substrates by reactive magnetron sputtering from 50 mm Cr target (99.95% pure) in Ar/O_2 plasma at a total pressure of 10^{-1} Pa. Distance between the substrate and the target was 55 mm. Deposition was performed in mixed Ar and O_2 atmosphere with 350 W radio

---

* Corresponding author.
E-mail address: pangxl@mater.ustb.edu.cn (K. Gao).

0040-6090/$ – see front matter © 2008 Elsevier B.V. All rights reserved.
doi:10.1016/j.tsf.2008.10.026

frequency (RF) power. Argon flow rate was kept at 15 standard cubic centimeters per minute (sccm), while oxygen flow rate was 6 sccm. Prior to coating deposition substrates were cleaned in acetone and ethanol for 10 min in order to remove organic contaminants, and then etched for 15 min in Ar plasma at RF power of 100 W to further clean the substrate surface. Chromium interlayer of 500 nm thick was sputtered for 10 min, after which oxygen gas was introduced into the sputtering chamber for the chromium oxide reactive sputter deposition, then 3 μm thick chromium oxide coating was deposited in 30 min. After that, the oxygen gas valve was shut down and next chromium interlayer was deposited. By repeating these steps Cr/Cr_2O_3 multi-layer structure was achieved. The substrate was electrically grounded and its temperature reached 473 K during deposition.

The coating microstructure was examined using Rigaku D/max-RB X-ray diffractometer with a Cu source ($\lambda = 1.54056$ Å). Each sample was exposed to the X-ray beam at 40 kV and 150 mA. The scanning region of the diffraction angle (2θ) was from 10° to 110° at 0.02° step size. TEM sample was prepared by FEI Focus Ion Beam (FIB) equipped with field emission scanning electron microscope. Tecnai F20 TEM was used to characterize interfaces and microstructure of chromium oxide multi-layers. TEM operating voltage was 200 kV. Fracture toughness was measured using Hysitron triboindenter and microhardness test instrument. Adhesion between chromium oxide coatings and steel substrates was evaluated by means of a scratch test using CETR Micro-Tribometer model UMT-2. The normal load was continuously increased at a rate of 0.25 N/s, while the conical diamond tip (120° angle, 200 μm tip radius) was moving at a constant velocity of 0.05 mm/s.

3. Results and discussion

Fig. 1 shows an FIB cut of the Cr/Cr_2O_3 coating multi-layer structure. A 500 nm metal chromium layer was deposited on high speed steel in order to achieve thick coating with low residual stress and good mechanical performance, then about 3 μm chromium oxide coating was deposited on top. Single Cr/Cr_2O_3 layer with the same thickness was deposited for the purpose of comparing the mechanical properties. The coating in Fig. 1(b) is quite dense without pores or inclusions present, so good mechanical properties can be expected. A metal interlayer between the substrate and the ceramic coating can help to relieve the residual stress and improve the coating fracture toughness, adhesion and impact resistance [17–19].

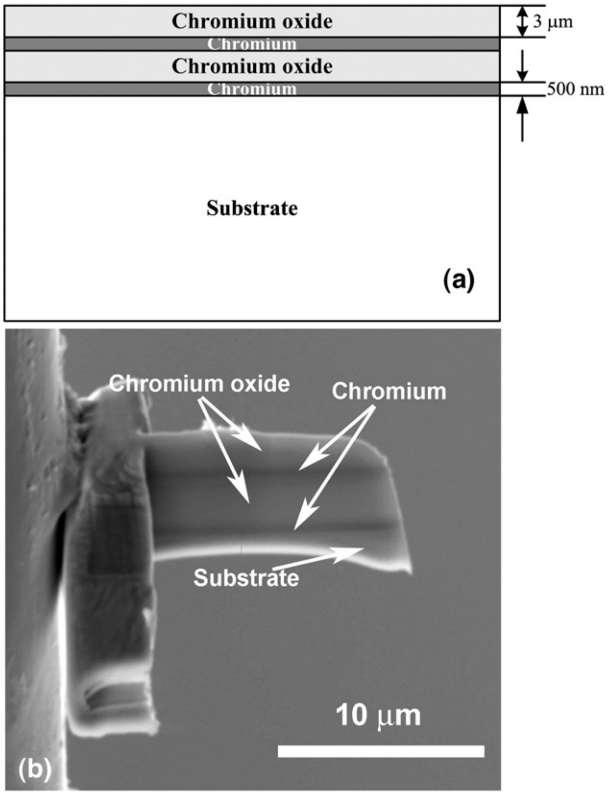

Fig. 1. (a) Multi-layer structure schematics; (b) FIB cross-section of the Cr/Cr_2O_3 multi-layer coating.

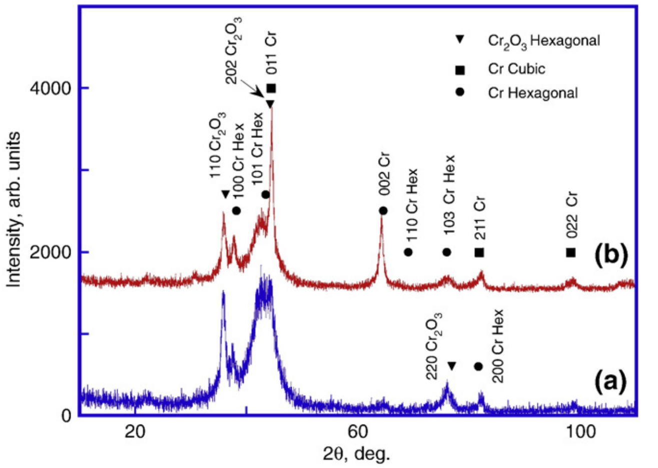

Fig. 2. XRD pattern of chromium oxide (a) single Cr/Cr_2O_3 layer; (b) multi-layer Cr/Cr_2O_3.

Considering the patterns measured in Fig. 2, the phase analysis of the single- and multi-layer chromium oxide coating samples was performed using a programme EVA [20] with direct link to the powder diffraction file [21]. The XRD patterns of the both samples show a lot of X-ray reflections attributed to Cr_2O_3 and cubic and hexagonal modifications of Cr (see Table 1). The XRD patterns were analysed by means of a programme ANALYZE [22]. The reflection profile data obtained (full width at half maximum (FWHM) *FWHM*, integral breadth β and central-angle Bragg angle $2\theta_B$ of the reflection profiles) were used for strain–size analysis of the samples.

As it is known, the broadening of the XRD reflection profiles can be caused by an influence of small-size incoherently diffracting crystallites formed due to presence of the dislocation arrays, stacking faults, twins and other extended imperfections. Additionally, the dislocations, vacancies, interstitials, substitutionals and other defects of this type result in formation of a strain in crystallites or in columns of the lattice unit cells. The strain and crystallite size broadening can be separated by integral breadth method as it is given briefly below.

The reflection profiles are described by Lorentzian function (Cauchy approximation) or by Gaussian function (Gaussian approximation) or by a combination of both reflection profile types (pseudo-Voigt function).

Table 1
Adopted from [39] structural data of the crystalline phases found in the samples

Crystalline phase	Space group[a]	*a* (Å)	*b* (Å)	*c* (Å)	Ref.
		α (°)	*β* (°)	*γ* (°)	
Cr, cubic	(229) $Im\bar{3}m$	2.885	*a*	*a*	ICSD code 64711
		90	90	90	
Cr, hexagonal	(194) $P6_3/mmc$	2.722	*a*	4.434	ICSD code 43526
		90	90	120	
Cr_2O_3	(167) $R\bar{3}c$	4.957	*a*	13.592	ICSD code 75577
		90	90	120	

[a] (Number of space group) space group symbol.

Table 2
Results of calculation of lattice strain and crystallite size[a]

	Model $t+\varepsilon$		Model t, $\varepsilon=0$		
Compound	Crystallite size t, nm	Strain ε, %	Crystallite size t, nm	Maximum penetration depth T, nm[b]	Miller indices *hkl* of reflections used for calculations
Single-layer sample 3000 nm Cr_2O_3/500 nm Cr/steel substrate					
Cr_2O_3	23.2(9)	0.43(4)	8.9(2.7)	6523	110, 220
	11.8(1.0)	0.60(10)	7.8(2.1)		
Cr (cubic)	–[c]	–[c]	8.5(3.7)	6920	011, 002, 112
			7.5(3.1)		
	–[c]	–[c]	6.5(1.8)	5600	011, 002
			5.8(1.6)		
Cr (hexagonal)	–	–	9.0(3.8)	3392	100, 103, 200
			8.2(3.3)		
Multilayer sample 2*(3000 nm Cr_2O_3/500 nm Cr)/steel substrate					
Cr_2O_3	18.4(2)	0.45(2)	8.2(2.2)	6523	110, 220
	10.3(8)	0.61(13)	7.2(1.7)		
Cr (cubic)	–[c]	–[c]	9.0(4.2)	7979	011, 002, 112, 022
			7.9(3.3)		
	47.8(1.4)	0.28(4)	15.6(2.6)	5600	011, 002
	19.5(2.0)	0.36(6)	12.9(1.7)		
	–[c]	–[c]	6.6(9)	7979	112, 022
			6.0(7)		
Cr (hexagonal)	–[c]	–[c]	10.2(3.8)	6434	100, 103, 200
			9.2(3.2)		

Nonspherical crystallites were assumed. Strain was assumed to be in unit cell columns perpendicular to the diffracting planes. First line represents results of calculations in the frames of Cauchy–Cauchy model for size and strain broadening. Second line gives results obtained using Gaussian–Gaussian approximation of the size and strain broadening. Most reliable data are underlined. Estimated standard deviations (e.s.d.) are shown in parenthesis.

[a] In the calculations the instrumental broadening was corrected using corresponding model of the profile broadening and data ($FWHM_{\mathrm{instr}}=0.100(5)°$) obtained for a reference Si powder (Standard Reference Material 640b of NIST). The e.s.d. of FWHM was $\Delta FWHM \approx 0.01°$. Taking into account a possible shift of the Bragg angles of the reflections, a high value of the uncertainty of the Bragg angles of the reflections $\Delta 2\theta = 0.5°$ was used for the calculations of the crystallite size and strain.

[b] Calculated assuming Cr_2O_3 top layer with effective coefficient of absorption $\mu_{\mathrm{eff}} = 0.5 * \mu\,(Cr_2O_{3\ \mathrm{crystalline}})$.

[c] Model is not consistent with experimental data.

According to [23], for Lorentzian-type reflection profiles the quantity

$$2W/\beta = 2/\pi = 0.63662,$$

whereas in case of the Gaussian reflection profiles

$$2W/\beta = 2^*(\ln(2))^{1/2}/\pi^{1/2} = 0.93949,$$

(here, $2W = FWHM$).

If reflection profile broadening caused by both, strain and size effects is described by Lorentzian-type, then a Cauchy–Cauchy model (often called the Williamson–Hall plot) is used for FWHM of the reflection profile:

$$FWHM = FWHM_{\mathrm{size}} + FWHM_{\mathrm{strain}}. \tag{1}$$

In case of Gaussian-type of the reflection broadening, Gaussian–Gaussian approximation is valid:

$$FWHM^2 = FWHM^2_{\mathrm{size}} + FWHM^2_{\mathrm{strain}} \tag{2}$$

Here, FWHM is corrected at instrumental broadening using corresponding approximation of the reflection profile.

The crystallite size contribution to the reflection profile broadening is calculated by Scherrer formula [24];

$$FWHM_{\mathrm{size}} = K^*\lambda/(t^*\cos(\theta_{\mathrm{B}})) \tag{3}$$

where $K=0.94$ if *FWHM* is used [25], λ is wave length of the X-ray radiation used and t is crystallite size.

For the strain component of the broadening:

$$FWHM_{\mathrm{strain}} = K_{\mathrm{strain}}{}^*\varepsilon^* tg(\theta_{\mathrm{B}}), \tag{4}$$

where ε is strain and $K_{\mathrm{strain}}=4$ for microstrain in crystallites and $K_{\mathrm{strain}}=5$ for strain in columns of the lattice unit cells perpendicular to diffracting lattice planes [26].

In our case the quantity $2W/\beta=0.67$. It is close to the value observed for Lorentzian reflection profiles and Cauchy–Cauchy approximation can be used for separation of the strain and size reflection profile broadening effect. Nevertheless, for comparison we have made the calculations using both, Cauchy–Cauchy and Gaussian–Gaussian approximations (Table 2). For the calculations, preferably not strongly overlapped reflections were used (if it was possible). To estimate the standard uncertainty of the calculations, a high value of the probable systematic deviation of about 0.5° was assumed for Bragg angles of the reflections (which cannot be corrected according to a reference reflection in our case). The instrumental broadening was estimated using a reference Si powder (Standard Reference Material 640b of NIST). As is seen from the Table 2, in agreement with $2W/\beta$-estimation the Cauchy–Cauchy approximation gives more reliable results with smaller uncertainty deviations (at least, for a model of simultaneous strain and crystallite size broadening). According to calculations, for both, single- and multi-layer samples, the broadening of the Cr_2O_3 reflection profiles is caused by both, size crystallite and strain effect. At the same time, for the Cr film the XRD reflections show the influence of the crystallite size effect only. We also investigated the effect of deposition parameters on preferred crystal orientation in previous work [27]. Some other researchers have proposed that the change in texture is often observed in transition metal oxide thin films with increasing thickness due to strain energy minimization [28,29], as the grains with lower strain energy grow at the expense of the highly strained ones. As is seen in Fig. 2, for the samples investigated both, Cr_2O_3 and hexagonal modification of Cr show a strong texture along [110] and [100] directions, respectively. As a result, a limited number of XRD reflections could be observed with mostly intensive ones (in comparison to theoretical intensities of the reflections according to [21]) of 110 and 220 reflections for Cr_2O_3 and 100 and 200 reflections of hexagonal Cr, correspondingly. At the same time, the cubic component of the chromium film shows a complete set of the XRD reflections of cubic Cr evidencing a good degree of polycrystallinity of this component which is a main component of the chromium film in agreement with higher intensity of the reflections in comparison to the hexagonal modification of Cr. In case of single-layer sample, the ratio of the reflection intensities I of the cubic Cr is comparable to theoretical one (for example, I_{011}/I_{112} is about 100/18 in comparison to theoretical value of 100/29 [21] for reflections 011 and 112). In agreement with higher volume of the metallic chromium films for multi-layer sample, the intensity of the XRD reflections of the cubic Cr is higher in comparison to single-layer sample (Fig. 2). However, in case of the multi-layer sample, the reflection intensity ratio is strongly distorted resulting in a high intensity of the 002 Cr reflection. Apparently, a preferred orientation along [001] direction of the cubic Cr modification is observed.

Microstructure of the coatings was analyzed with scanning TEM using bright and dark field imaging. Fig. 3(a) shows the multi-layer Cr/Cr_2O_3 coatings microstructure on steel substrate. The top layer is chromium oxide, which was almost removed by Ga ions milling during TEM sample preparation in the FIB. This chromium oxide layer has columnar grain structure. Zone A was enlarged to get a clear view of the microstructure of the top chromium oxide layer in Fig. 3(b). Comparing bright and dark images of zone A, it is clear that there is a 'V-shaped' columnar grain structure, and the grain size increases with the film thickness. This is consistent with our previous results obtained from the single Cr/Cr_2O_3 layer [17]. Probably, the formation of the columnar grain structure in the volume of the chromium oxide film gives rise to an appearance of the strain in the columnar grains and a texture of the film as it is detected above in XRD investigations.

Fig. 3(c) and (d) shows the metal chromium microstructure and interfaces of chromium oxide coating and the chromium interlayer. In these figures, 'V-shaped' metal chromium columnar structure is also observed but in some zones only. As a result, no strain was found in metallic chromium films and texture of the main component (cubic Cr modification) is rather small as it is discussed above. The grain size of metal chromium layer changed from about 10 nm at the bottom to 50 nm at the top of the interlayer. TEM grain size measurements are in agreement with the X-ray results from Table 2. Based on the empirical Hall–Petch relationship, the yield strength of polycrystalline metals is generally observed to decrease as the grain size increases [30,31]:

$$\sigma_y = \sigma_0 + k_d d^{-1/2}, \qquad (5)$$

where d is the grain diameter, σ_y is the yield strength, σ_0 and k_d are material-dependent constants. A physical basis for this behavior is associated with the difficulty of dislocations movement across grain boundaries and stress concentration due to dislocations pile-up. The hardness also has been found to decrease with increasing grain size, which also scales with $d^{-1/2}$ [32], so there should be an optimal thickness of metal interlayer for ceramic hard coatings to achieve good mechanical properties [17].

It was also detected that there are some amorphous or random polycrystalline grains at the interfaces between the metal interlayer, chromium oxide coatings and steel substrate in Fig. 3(d) and (e), which were probably induced by the lattice mismatch. This coating was deposited at around 200 °C, which is less than 0.1 of the melting temperature, resulting in non-equilibrium and kinetically limited growth processes, especially at the beginning of the deposition, so amorphous and random polycrystalline grains were formed at the interfaces. Amorphous layers also allow relieving the growth stress in the coating. Chromium oxide coatings can have high residual stress, which leads to thicker coatings failures [17]. We also investigated the effects of annealing on the microstructure and mechanical properties of chromium oxide coatings, and found that an amorphous to crystalline phase transformation can be observed at certain conditions, which actually improves the coating mechanical properties [33].

Fracture toughness of thin films can be measured by various methods, such as buckling test, chipping and indentation tests. Indentation test is a popular method for thin film fracture toughness

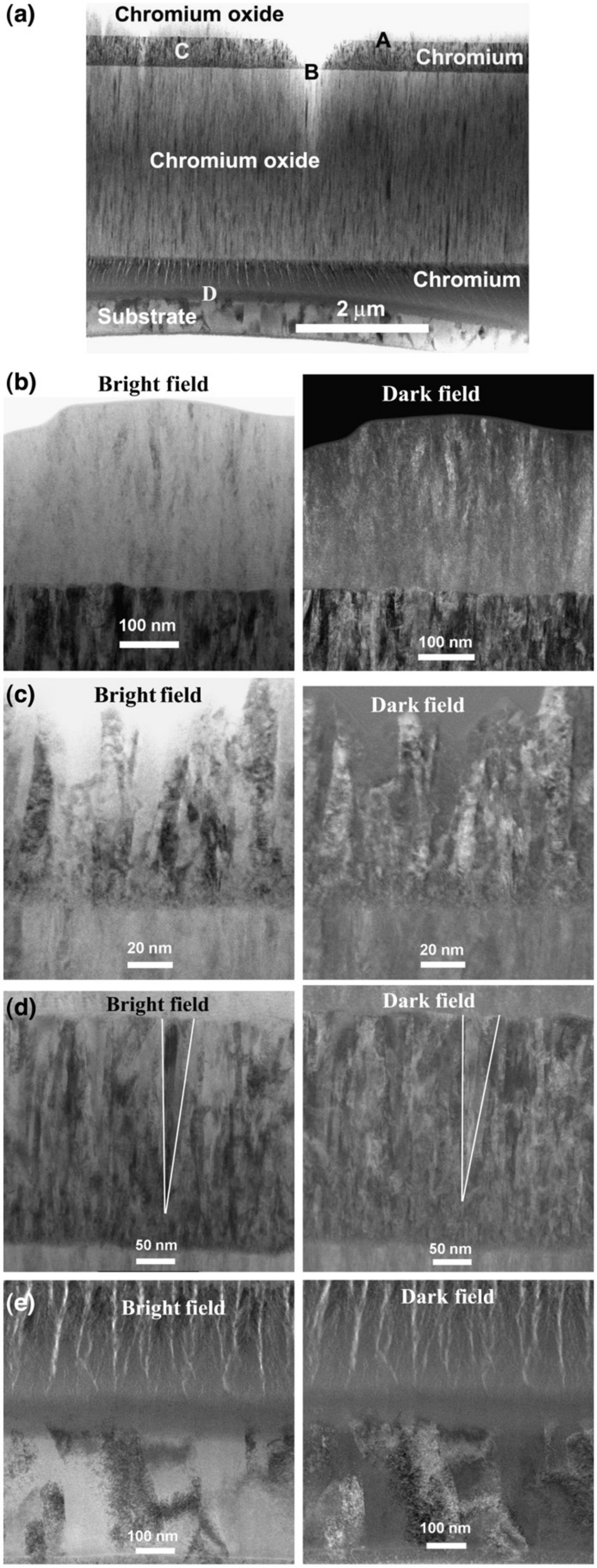

Fig. 3. (a) STEM images of multi-layer Cr/Cr_2O_3 structure; (b) Bright and dark field images of zone A; (c) Bright and dark field images of zone B; (d) Bright and dark field images of zone C; (e) Bright and dark field images of zone D.

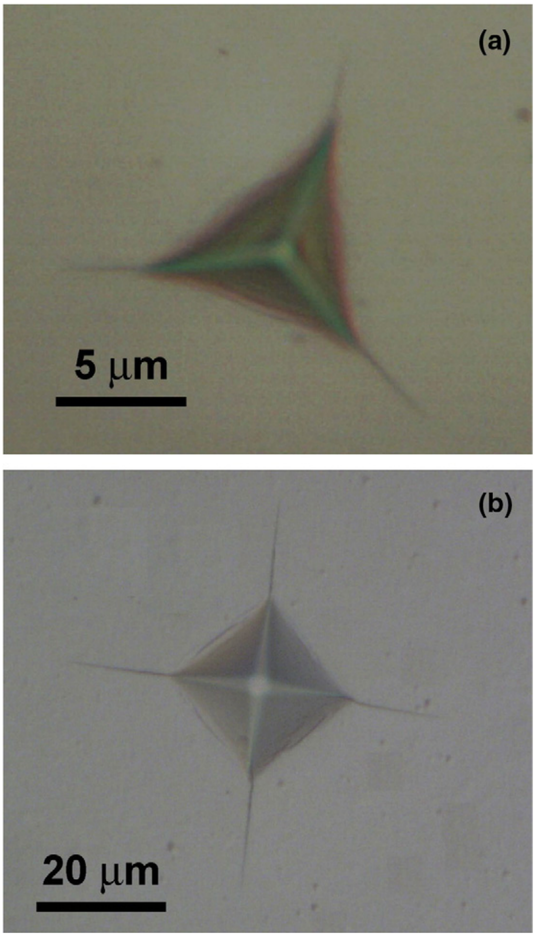

Fig. 4. Optical micrographs of indentation-induced fracture in chromium oxide coating: (a) Berkovich indenter; (b) Vickers indenter.

measurement. Fig. 4 shows indents and the resulting radial cracks in chromium oxide coating produced by Berkovich and Vickers indenter tips. Lawn and Marshall [33] have shown that a simple relationship exists between the fracture toughness, K_c, and the length of the radial cracks, c:

$$K_c = \alpha \left(\frac{E}{H}\right)^{1/2} \left(\frac{P_{\max}}{c^{3/2}}\right) \qquad (6)$$

Here, $P_{\max}$ is the peak indentation load and α is an empirical constant, which depends on the indenter geometry. The constant was found to be 0.016 for Berkovich and 0.039 for the Vickers indenter, while it is 0.032 for the Cube-corner indenter [34,35]. H is the mean hardness, and E is the elastic modulus, which can be calculated using the following equation [36]:

$$\frac{1}{E_r} = \frac{1-\nu_{\text{Sample}}^2}{E_{\text{Sample}}} + \frac{1-\nu_{\text{Tip}}^2}{E_{\text{Tip}}} \qquad (7)$$

where E and ν are the elastic modulus and Poisson's ratio of diamond tip with the values of 1140 GPa and 0.07, respectively. The fracture toughness of our single and multi-layer Cr/Cr_2O_3 coating is between 4.04 and 5.97 MPa·m$^{1/2}$ measured with the Berkovich indenter, and between 2.81 and 3.91 MPa·m$^{1/2}$ when measured with the Vickers indenter. All reported values of the K_c measured using the indentation test represent the average of eight indents. In Fig. 4(b) one can see that radial cracks are not the only form of energy release, as other types of cracks are present. There are some small annular cracks around the indentation, which explains why the values of fracture toughness measured by Berkovich and Vickers indenters are a little different. The difference of fracture toughness values between single and multi-

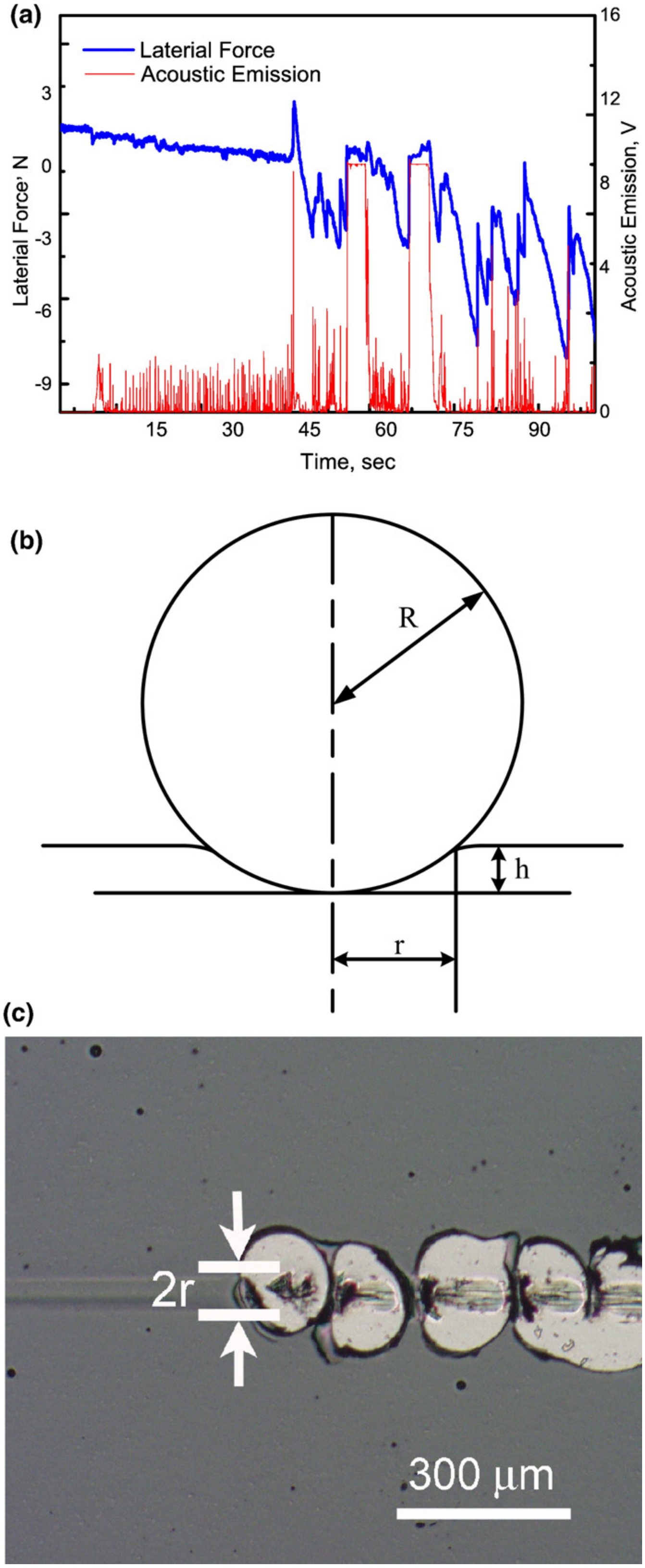

Fig. 5. (a) Acoustic emission and lateral force change used to determinate the coating critical failure point during the scratch test; (b) schematic representation of scratch contact radius; (c) Scratch scar optical image.

layer coatings is due to the difference in intrinsic stresses and the amounts of stored elastic energy due to the presence of the metal chromium interlayer.

Adhesion is one of the most important properties for films and coatings and can be assessed with the scratch test, although there is a problem with this method in terms of defining the critical normal force. Fig. 5(a) shows the lateral force and acoustic emission signal obtained during a scratch test. The critical lateral load is easily identified from the increased acoustic emission signal. The normal force was increased linearly during the scratch testing, so it was easily calculated at the critical coating delamination point and the critical normal load. The average value of the critical normal load was 13.3 and 15.2 N for single and multi-layer Cr/Cr_2O_3, gained from three scratches on each sample, respectively. The adhesion was calculated using Eq. (8):

$$P_c = \frac{\pi r^2}{2}\left(\frac{2EW_A}{h}\right)^{1/2} \tag{8}$$

where r is the contact radius determined from the width of the scratch track at the critical normal load (Fig. 5(b) and (c)), and h is the coating thickness [37,38]. The adhesion is about 192.1 and 246.7 J/m^2 for single and multi-layer Cr/Cr_2O_3, respectively. The main reason for the difference of adhesion for single and multi-layer Cr/Cr_2O_3 is that the residual stress in the coatings is quite different because of the extra chromium interlayer, which reduces the amount of stored elastic energy in the coating, and increases the adhesion.

4. Conclusions

Single and multi-layer Cr_2O_3 coatings exhibit different crystallographic preferred orientation for the same deposition conditions, based on the XRD results. TEM analysis shows that both metal chromium interlayer and ceramic chromium oxide have 'V-shaped' columnar microstructure, where the grain size increases with the film thickness. The fracture of single and multi-layer coatings shows some differences when tested with the Berkovich and the Vickers indenters. The values of single and multi-layer fracture toughness are between 4 and 6 $MPa \cdot m^{1/2}$ measured with the Berkovich tip, and are between 2.8 and 3.9 $MPa \cdot m^{1/2}$ when measured with the Vickers indenter. The adhesion also shows some differences between single and multi-layer coatings; it is about 192.1 and 246.7 J/m^2, respectively.

Acknowledgements

This work was supported by the National Natural Science Foundation of China (No. 50471091). Alex Volinsky would like to acknowledge support from NSF under grants CMMI-0600266 and CMMI-0600231.

References

[1] U. Rothhaar, H. Oechsner, Thin Solid Film 302 (1997) 266.
[2] P. Hones, M. Diserens, F. Levy, Surf. Coat. Technol. 120/121 (1999) 277.
[3] E. Sourty, J.L. Sullivan, M.D. Bijker, Trib. Int. 36 (2003) 389.
[4] F. Lai, C. Huang, C. Chang, L. Wang, W. Cheng, Microelectronic Eng. 67/68 (2003) 17.
[5] T. Seike, J. Nagai, Sol. Energy Mater. 22 (1991) 107.
[6] J.C. Nable, S.L. Suib, F.S. Galasso, Surf. Coat. Technol. 186 (2004) 423.
[7] V.M. Bermudez, W.J. DeSisto, J. Vac. Sci. Technol. A 19 (2001) 576.
[8] G. Goodlet, S. Faty, S. Cardoso, P. Freitas, A. Simoes, M. Ferreira, M. Belo, Corros. Sci. 46 (2004) 1479.
[9] S. Hong, E. Kim, D. Kim, T. Sung, K. No, J. Non-Cryst. Solids 221 (1997) 245.
[10] D. Gall, R. Gampp, H.P. Lang, P. Oelhafen, J. Vac. Sci. Technol. A 14 (1996) 374.
[11] J.D. Kruschwitz, W.T. Pawlewicz, Appl. Opt. 36 (1997) 2157.
[12] T. Seike, J. Nagai, Sol. Energy Mater. 22 (1991) 107.
[13] C. Sunseri, S. Piazza, F.D. Quarto, J. Electrochem Soc. 137 (1990) 2411.
[14] R.H. Misho, W.A. Murad, G.H. Fattahallah, Thin Solid Films 169 (1989) 235.
[15] K.D. Bouzakis, S. Hadjiyiannis, G. Skordaris, I. Mirisidis, N. Michailidis, G. Erkens, Surf. Coat. Technol. 188/189 (2004) 636.
[16] J.H.W. Siu, K.Y. Li, Wear 237 (2000) 283.
[17] X. Pang, K. Gao, H. Yang, L. Qiao, Y. Wang, A. Volinsky, Adv. Eng. Mater. 9 (2007) 594.
[18] G. Kim, S. Lee, J. Hahn, B. Lee, J. Han, J. Lee, S. Lee, Surf. Coat. Technol. 171 (2003) 83.
[19] A. Leyland, A. Matthews, Surf. Coat. Technol. 70 (1994) 19.
[20] DIFFRACplus Evaluation package (EVA), Release 2001, Bruker AXS GmbH, 2001.
[21] Powder diffraction file (PDF), Release 2001, International Centre for Diffraction Data (ICSD), 2001.
[22] Programm ANALYZE, Rayflex Version 2.285, Rich. Seifert & Co., 2000.
[23] J.I. Langford, Accuracy in Powder Diffraction, National Bureau of Standards, Special Publication, vol. 567, 1980, pp. 255–269.
[24] R.A. Young, A. Sakthivel, T.S. Moss, C.O. Paiva-Santos, J. Appl. Cryst. 28 (1995) 366.
[25] J.I. Langford, J. Appl. Cryst. 11 (1978) 10.
[26] A.R. Stokes, A.J. Wilson, Proc. Phys. Soc. London 56 (1944) 174.
[27] X. Pang, K. Gao, A. Volinsky, J. Mater. Res. 22 (2007) 3531.
[28] S. Lim, D. McCulloch, M. Bilek, D. McKenzie, J. Appl. Phys. 93 (2003) 4283.
[29] J. Greene, J. Sundgren, L. Hultman, I. Petrov, D. Bergstrom, Appl. Phys. Lett. 67 (1995) 2928.
[30] E. Hall, Proc Phys Soc London, Sect B 64 (1951) 747.
[31] N. Petch, J. Iron Steel Inst., London 174 (1953) 25.
[32] J. Chen, L. Lu, K. Lu. Scripta Mater. 54 (2006) 1913.
[33] X. Pang, K. Gao, H. Yanng, L. Qiao, A.A. Volinsky, Thin Solid Films 516 (2008) 4685.
[34] B. Bhushan, X.D. Li, Int. Mater. Rev. 48 (2003) 125.
[35] X.D. Li, D.F. Diao, B. Bhushan, Acta Mater. 45 (1997) 4453.
[36] K.L. Johnson, Contact Mechanics, Cambridge Press, Cambridge, 1985.
[37] A.A. Volinsky, N.R. Moody, W.W. Gerberich, Acta Mater. 50 (2002) 441.
[38] X. Hernot, O. Bartier, Y. Bekouche, R. El Abdi, G. Mauvoisin, Int. J. Solids Struct. 43 (2006) 4136.
[39] Inorganic Crystal Structure Database (ICSD), Release 2008-1, FIZ/NIST, 2008.